ELECTROCHEMISTRY

Systems-level investigation of aqueous batteries for understanding the benefit of water-in-salt electrolyte by synchrotron nanoimaging

Cheng-Hung Lin[1]*, Ke Sun[1]*†, Mingyuan Ge[2], Lisa M. Housel[3], Alison H. McCarthy[1], Mallory N. Vila[3], Chonghang Zhao[1], Xianghui Xiao[2], Wah-Keat Lee[2], Kenneth J. Takeuchi[1,3], Esther S. Takeuchi[1,3,4], Amy C. Marschilok[1,3,4], Yu-chen Karen Chen-Wiegart[1,2]†

Water-in-salt (WIS) electrolytes provide a promising path toward aqueous battery systems with enlarged operating voltage windows for better safety and environmental sustainability. In this work, a new electrode couple, LiV_3O_8-$LiMn_2O_4$, for aqueous Li-ion batteries is investigated to understand the mechanism by which the WIS electrolyte improves the cycling stability at an extended voltage window. Operando synchrotron transmission x-ray microscopy on the $LiMn_2O_4$ cathode reveals that the WIS electrolyte suppresses the mechanical damage to the electrode network and dissolution of the electrode particles, in addition to delaying the water decomposition process. Because the viscosity of WIS is notably higher, the reaction heterogeneity of the electrodes is quantified with x-ray absorption spectroscopic imaging, visualizing the kinetic limitations of the WIS electrolyte. This work furthers the mechanistic understanding of electrode–WIS electrolyte interactions and paves the way to explore the strategy to mitigate their possible kinetic limitations in three-dimensional architectures.

INTRODUCTION

Li-ion batteries and beyond-Li systems based on aqueous electrolytes could be an attractive alternative to current Li-ion battery technology due to improved safety with lower risk of fire and decreased environmental impact (*1*, *2*). However, the limited voltage window for water of ~1.23 V has impeded the development of practical high-voltage aqueous battery technology for more than 20 years. Through fine-tuning of pH values and other electrolyte parameters, stable cycling of some electrode couples in aqueous Li-ion batteries such as $LiMn_2O_4$-$LiTi_2(PO_4)_3$ and $LiMn_2O_4$-TiP_2O_7 with cell voltages of ~1.5 V has been realized (*3*–*5*). However, the voltage range is still far from being competitive, with commercial Li-ion batteries with nonaqueous electrolytes operating at >3.5 V.

The perspective that water-based electrolyte cannot sustain a working voltage window greater than ~1.5 V has remained unchallenged until recently, when a new concept of water-in-salt (WIS) electrolyte was introduced (*6*–*10*). The WIS electrolyte is an electrolyte in which the molality of salts in water is so high that the salt outnumbers the water solvent in the system by both weight and volume (*6*) and that all water molecules are coordinated with the metal cations while retaining their fluidity (*9*). The literature showed that when the lithium bis(trifluoromethanesulfonyl)imide (LiTFSI) concentration is above 5 m (mol kg^{-1}), the WIS definition applies (*6*), and the WIS electrolyte with an even higher concentration of salts [e.g., 20 m (mol kg^{-1}) of LiTFSI and lithium bis(pentafluoroethanesulfonyl)imide (LiBETI) or higher] has been demonstrated with superior performance than the dilute aqueous electrolyte (*6*, *9*). The use of these high-concentration Li salts in the electrolyte increases the voltage window of the aqueous electrolyte substantially based on the Nernst equation (*6*). In addition, the high salt concentration increases the chemical potential of the anion of the lithium salt in the electrolyte by affecting both the concentration and activity coefficient terms in the activity calculation (*9*). This substantial increase in the anion chemical potential enhances anode surface passivation, where a dense and inert LiF-based passivation film on the anode particle surface has been observed. This is regarded as an inorganic version of the anode surface electrolyte interphase (SEI) present in nonaqueous Li-ion batteries (*6*). Both the thermodynamically stable potential and kinetically suppressing side reactions with passive SEI from the WIS electrolyte combine to extend the voltage window, enabling relatively stable cycling of 2- and even 4-V electrode with specific WIS electrolyte formulations (*11*). Recent work further demonstrated that more cost-effective and nontoxic salts can be used in the WIS electrolyte for aqueous Li-ion battery (*12*) as well as proof-of-concept work of WIS used in the range of beyond-Li systems including Li-O_2 battery (*13*), Na-ion battery (*14*), K-ion battery (*15*), dual-ion batteries (*16*), and supercapacitors (*17*). The WIS electrolyte concept has thus opened a new research direction in energy storage and conversion for future safer and more environmentally friendly systems.

The WIS electrolyte concept represents a major breakthrough, and research efforts have been following this direction to explore the capability and limits of WIS systems. To date, beyond the demonstration or electrochemical performances, most of the characterization has focused on specific cell components, such as the electrolyte and electrode particles (*6*, *8*–*10*). It is also important to characterize the battery with the WIS electrolyte at a systems level to probe the behavior of cell components in the WIS electrolyte. In particular, direct visualization of aqueous Li-ion batteries by operando methods to compare their morphological evolution in the WIS electrolyte with the conventional lower concentration electrolytes has yet to be

[1]Department of Materials Science and Chemical Engineering, Stony Brook University, Stony Brook, NY 11794, USA. [2]National Synchrotron Light Source II, Brookhaven National Laboratory, Upton, NY 11973, USA. [3]Department of Chemistry, Stony Brook University, Stony Brook, NY 11794, USA. [4]Energy and Photon Sciences Directorate, Brookhaven National Laboratory, Upton, NY 11973, USA.
*These authors contributed equally to this work.
†Corresponding author. Email: karen.chen-wiegart@stonybrook.edu (Y.-c.K.C.-W.); sunke612@gmail.com (K.S.)

conducted, which is critical to provide further insights into the reaction mechanisms of the WIS system for future innovation.

Transmission x-ray microscopy (TXM) conducted at advanced synchrotron x-ray light sources is a powerful characterization technique that provides a large field of view on the order of tens of micrometers and also offers a relatively high spatial resolution, as low as ~30 nm for hard x-rays (*18*–*20*). A tunable incident x-ray energy at the synchrotron light source further enables x-ray absorption spectroscopy to be combined with the x-ray nanoimaging in two dimension (2D) and 3D for both elemental and chemical mapping; this spectroscopic imaging capability, also known as x-ray absorption near-edge structure (XANES) spectroscopic imaging, is valuable to understand the reaction dynamics of both chemical and electrochemical systems (*19*, *21*–*27*).

The work presented here demonstrates a new cathode-anode system for bisalt WIS (*9*) using LiV_3O_8-$LiMn_2O_4$ as an aqueous electrode couple. The bisalt can increase the solubility of Li salts in H_2O through the eutectic effect to maximize the concentration difference between a WIS electrolyte and an electrolyte with normal salt concentration. Both the thermodynamic and kinetic stability window of the water-based electrolyte can be further extended with respect to the single-salt WIS electrolyte (*9*). $LiMn_2O_4$ is a commonly used cathode material in aqueous Li-ion battery studies due to its high voltage and high capacity. Thus, the morphological evolution and reaction dynamics of $LiMn_2O_4$ in the WIS electrolyte, compared with conventional low-salt concentration aqueous electrolyte, are important subjects to be studied. In choosing an anode material to be paired with $LiMn_2O_4$, LiV_3O_8 is a highly suitable anode material for the study of aqueous Li-ion batteries. The reasons are threefold: First, LiV_3O_8 has a moderate voltage window and an average redox voltage of ~3 V versus Li/Li^+ during lithium intercalation/deintercalation, allowing LiV_3O_8 to be cycled within the stable window of water (*2*). Notably, with the WIS electrolyte, the cycling window of LiV_3O_8 can be extended further to use its capacity to a greater extent, demonstrated in this study. Second, its high theoretical capacity of 372 mAh g^{-1} and demonstrated achievable capacity of >200 mAh g^{-1} are an advantage when compared with other anode materials for aqueous Li-ion batteries. Third, the material is an excellent choice to achieve high benefit from the TXM experiment. The distinctively different morphology of our synthesized LiV_3O_8 (*28*, *29*) compared to $LiMn_2O_4$ and low x-ray absorption are important considerations for the experimental design. These two factors enable the differentiation of the $LiMn_2O_4$ component from the LiV_3O_8 during the operando TXM study, which is the emphasis of this work.

This work applies operando x-ray nanoimaging using TXM to probe aqueous Li-ion batteries with different electrolytes: both high-concentration WIS electrolyte and conventional aqueous electrolyte with lower salt concentration (Fig. 1). The operando TXM nanoimaging provides direct evidence for the stability of the WIS electrolyte compared to the conventional aqueous electrolyte composition when operating under high voltages. However, the x-ray absorption spectroscopic imaging by TXM also reveals the relatively homogeneous chemical states of the WIS electrolyte at modest rates and electrode thicknesses, elevating concerns with kinetic limitations due to the high viscosity under relevant conditions. Overall, this work opens new directions on using state-of-the-art characterization techniques to probe the morphological and chemical evolution of WIS systems while revealing a new reaction couple, LiV_3O_8-$LiMn_2O_4$, suitable for aqueous Li-ion batteries.

RESULTS AND DISCUSSION

Electrode characterizations

The structure of as-synthesized LiV_3O_8 powder was first determined by x-ray powder diffraction (XRD), as shown in fig. S1A. All the major peaks can be assigned to the LiV_3O_8 phase [powder diffraction file (PDF) 01-073-8145] with the $P2_1/m$ space group. The morphology of the LiV_3O_8 powder is shown in the scanning electron microscopy (SEM) image in fig. S1B, which has the bar-like shape consistent with what is predicted by density functional theory simulation (*28*). The lithiation-delithiation voltage profiles of LiV_3O_8 in nonaqueous electrolyte against lithium anode at different rates are shown in fig. S1C, which resembles that of $Li_{1.1}V_3O_8$ in both shape and capacity delivered as demonstrated in previous work (*28*). From fig. S1C, it is evident that the reaction of LiV_3O_8 with lithium is reversible and can provide reasonable capacity for rates as high as 5 C. Although as an anode for the aqueous Li-ion battery its output voltage (~2.5 V on average) is relatively high, it is similar to the Mo_6S_8 anode previously reported for the WIS electrolyte (*6*). Furthermore, the small hysteresis between the charge and discharge shown in fig. S1C at different rates is an advantage of this material as an anode.

The cathode paired with the LiV_3O_8 anode is $LiMn_2O_4$ obtained commercially. The XRD pattern of the $LiMn_2O_4$ powder is shown in fig. S2A. Most of the peaks belong to the spinel $LiMn_2O_4$ phase

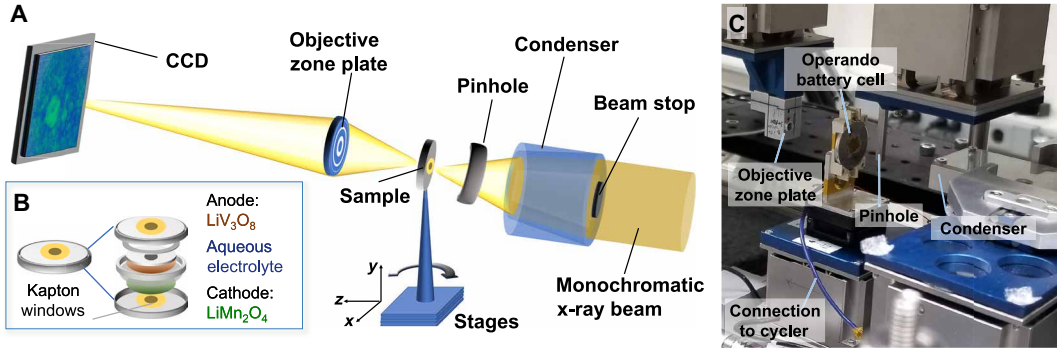

Fig. 1. Experimental setup for operando TXM imaging of LiV_3O_8-$LiMn_2O_4$ aqueous Li-ion batteries. (**A**) Schematic showing the experimental layout. CCD, charge-coupled device. (**B**) Operando cell design and key components. (**C**) Photo of the operando TXM experiment. Photo credit: Yu-chen Karen Chen-Wiegart, Stony Brook University and Brookhaven National Laboratory.

(PDF 00-35-0782) with the *Fd*-3*m* space group, with a minor impurity Mn_2O_3 (PDF 00-41-1442). Because Mn_2O_3 does not contain lithium, it will not participate in the initial delithiation process during the charge and thus stay as an inactive component in the cathode. The SEM image of $LiMn_2O_4$ powder is shown in fig. S2B, which has a distinctively different spherical morphology from LiV_3O_8 but similar in size (~1 to 10 μm). The voltage profile of $LiMn_2O_4$ charged and discharged between 4.5 and 3.3 V is shown in fig. S2C. The two voltage plateaus at 4.1 and 3.95 V correspond to the two different reaction regions with two-phase (4.1 V) and single-phase (3.95 V) reaction mechanisms (*30*).

Electrochemistry of LiV_3O_8-$LiMn_2O_4$ in conventional and WIS aqueous electrolytes

The first-cycle voltage profile of a LiV_3O_8-$LiMn_2O_4$ cell when charged at 0.1 C is shown in Fig. 2A for the WIS electrolyte and the 1 M (mol L^{-1}) (1.2 m) LiTFSI:LiBETI electrolytes, respectively. In the case of the 1 M LiTFSI:LiBETI electrolyte, the cell enters into an indefinite voltage plateau after it reaches around 1.95 V. This behavior is likely due to the decomposition of water, of which the thermodynamic voltage window is only 1.23 V (*6*). In contrast, with the WIS electrolyte, the LiV_3O_8-$LiMn_2O_4$ cell can reach 2.5 V without experiencing the long charge plateau observed in the 1 M LiTFSI:LiBETI electrolyte case. This is consistent with the recent literature results, which established that the WIS electrolyte extends the voltage window of water by shifting its oxidation voltage to higher values thermodynamically and passivating the anode with an SEI layer. During the discharge, the capacity delivered by the cell WIS electrolyte does not fully match its charge capacity. The low coulombic efficiency in the first cycle may be due to the formation of SEI layer on the anode, which has been consistently observed in previous literature for the WIS systems (*6*, *8*–*10*). The cycling of the WIS electrolyte cell at 0.1 C is shown in Fig. 2B, which demonstrates capacity fading in the first 10 cycles. Although the low rate tests between 2.5 and 0.3 V did not fully reproduce those presented in the original study with the same WIS electrolyte formulation (*9*), overall, the significant improvement of the electrochemical stability with the WIS electrolyte is consistent.

At a higher rate (1 C), both the WIS and the 1 M LiTFSI:LiBETI electrolytes allow the LiV_3O_8-$LiMn_2O_4$ couple to be cycled between 2.0 and 0.3 V, as shown in Fig. 2C. From Fig. 2D, the cycling stability of the WIS electrolyte is much better than the conventional 1 M LiTFSI:LiBETI electrolyte in both capacity retention and coulombic efficiency; after 20 cycles, the discharge capacity of the WIS electrolyte was still kept at 73 mAh g^{-1}, which was ~7% lower than the beginning, whereas the capacity of 1 M electrolyte was only 45 mAh g^{-1}, which has an ~50% decrease as compared to the first cycle. This also supports the idea that the WIS electrolyte has better stability than the conventional aqueous electrolyte with lower salt concentration.

Surface morphological and elemental evolution in conventional and WIS aqueous electrolytes

To gain further understanding of the enhanced stability of the WIS electrolyte in the LiV_3O_8-$LiMn_2O_4$ electrode couple cell, we performed

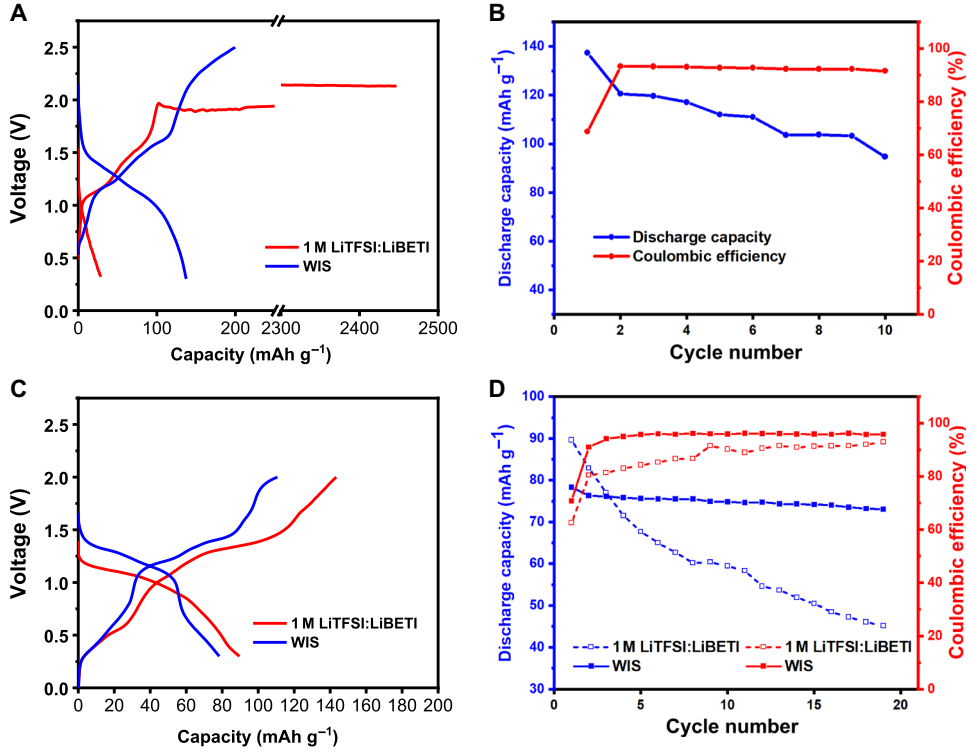

Fig. 2. Electrochemical performance of the LiV_3O_8-$LiMn_2O_4$ couple. (**A**) Voltage profile of the 1 M LiTFSI:LiBETI electrolyte cell and the WIS electrolyte cell at 0.1 C during the first charge and discharge between 2.5 and 0.3 V. (**B**) Cycling behavior of the WIS electrolyte cell at 0.1 C between 2.5 and 0.3 V. (**C**) Voltage profile of the 1 M LiTFSI:LiBETI electrolyte cell and the WIS electrolyte cell at 1 C during the first charge and discharge between 2.0 and 0.3 V. (**D**) Cycling behavior of the WIS electrolyte cell at 1 C between 2.0 and 0.3 V. The rates are normalized by the capacity of the $LiMn_2O_4$ cathode, and the gravimetric capacity values are normalized by the mass of $LiMn_2O_4$.

SEM on the postcycled electrodes from different electrolyte chemistries. The SEM images are shown in Fig. 3 (A to F) for the $LiMn_2O_4$ cathode and Fig. 3 (H to M) for the LiV_3O_8 anode. The electrode samples from the 1 M (1.2 m) LiTFSI:LiBETI electrolyte cell have been cycled with one full cycle, of charge and discharge at a rate of 0.1 C. The charge time is ~72 hours due to the indefinite charging behavior shown in Fig. 2A. The electrode samples for the WIS electrolyte were obtained from a cell in fully discharged state after being cycled at a rate of 0.1 C between 2.5 and 0.3 V for 10 cycles, and the total time of cycling was about 160 hours.

In Fig. 3 (A to F), the most notable difference between the 1 M LiTFSI:LiBETI electrolyte and the WIS electrolyte can be observed in the $LiMn_2O_4$ cathode. Comparing the morphology of the cell cycled in 1 M electrolyte (Fig. 3, B and E; higher-resolution image is shown in fig. S8, A and B) to the one cycled in the WIS electrolyte (Fig. 3, C and F), it can be observed that the morphology of the $LiMn_2O_4$ electrode from the WIS electrolyte cell, especially the spherical electrode particles, remains similar to the morphology of the pristine $LiMn_2O_4$ electrode (Fig. 3, A and D). On the contrary, the morphology of the spherical $LiMn_2O_4$ particles changed significantly in the cycled electrode from the 1 M LiTFSI:LiBETI electrolyte cell: The initial particles have smooth surfaces with well-defined facets (Fig. 3D); this smooth particle surface transformed into a mossy and fibrous one, which indicates a significant damage of the $LiMn_2O_4$ particles' surfaces during cycling in the dilute 1 M LiTFSI:LiBETI electrolyte.

In comparison, the morphological change of the anode is not as notable as the cathode. As shown in Fig. 3 (H to M), after the cycling, the LiV_3O_8 particles tested in the two electrolytes both maintain the overall rectangular shape with the well-defined crystal edge and corners. A small amount of surface deposition was observed on the LiV_3O_8 particles from the 1 M LiTFSI:LiBETI electrolyte cell (Fig. 3L), which is not seen in its WIS electrolyte counterpart (Fig. 3M). However, the difference observed in the anode between the two different electrolytes is smaller than that observed in the cathode case, as shown in Fig. 3 (A to F). The SEM analysis indicates that most of the damage on the active electrode particles is experienced by the cathode $LiMn_2O_4$ materials during the water-involved side reactions with the 1 M LiTFSI:LiBETI electrolyte. In the meantime, the WIS electrolyte is effective in suppressing the damage done on the $LiMn_2O_4$ cathode particles by the side reactions.

Energy-dispersive x-ray spectroscopy (EDS) spectra were also collected on the electrodes in Fig. 3 (A to F and H to M) and are shown in Fig. 3 (G and N). In both Fig. 3 (G and N), the S peak is attributed to the residue LiTFSI:LiBETI electrolyte salts remaining on the electrodes. The Si peak is the internal fluorescence peak resulting from the Si EDS detector (*31*). The Al signal is a background signal coming from the SEM/EDS sample holder, which is made of Al. Besides, on the LiV_3O_8 electrodes in Fig. 3N, the major V kα peak and other elements' peaks shared by all three different samples, Mn Kα peak is also observed on the LiV_3O_8 electrode from the 1 M LiTFSI:LiBETI electrolyte cell. However, there is no Mn Kα peak observed on the LiV_3O_8 electrode cycled in the WIS electrolyte. This suggests that the $LiMn_2O_4$ cathode experienced substantial dissolution in the 1 M LiTFSI:LiBETI electrolyte during the cycling,

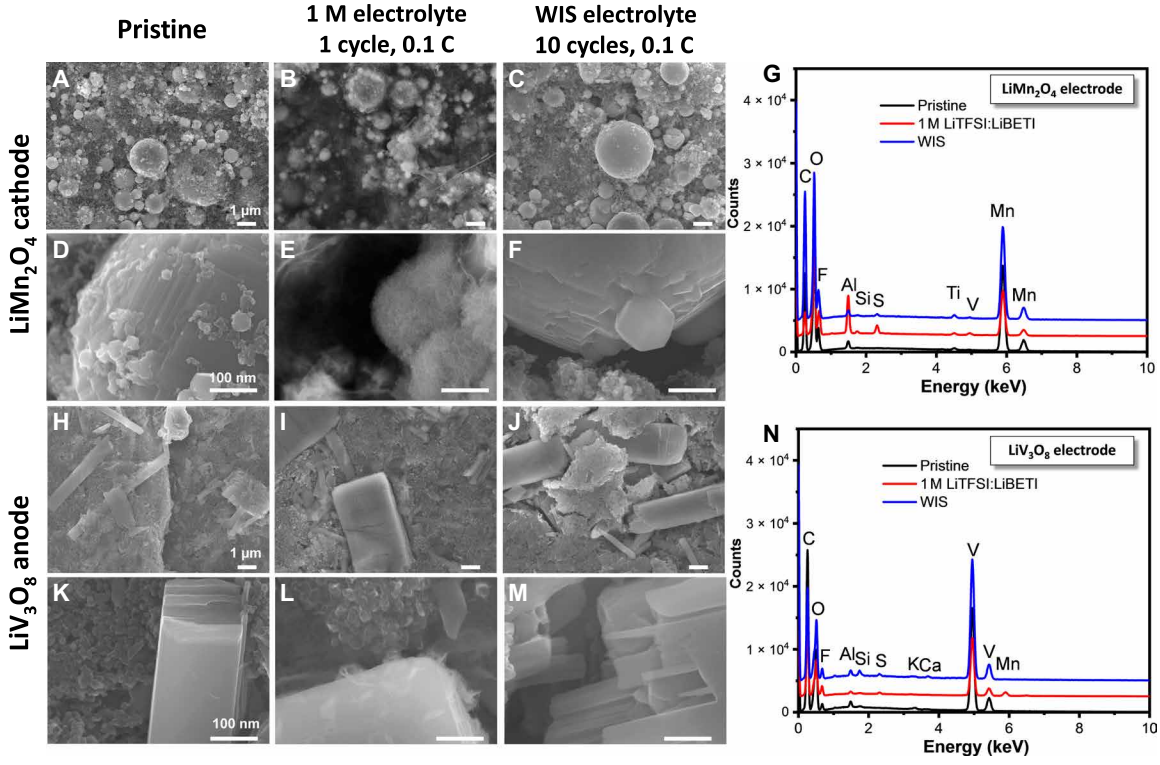

Fig. 3. SEM and EDS characterizations of pristine and post-cycled electrodes. Surface morphological evolution of (**A** to **F**) the $LiMn_2O_4$ cathode and (**H** to **M**) the LiV_3O_8 anode. (A and H) Pristine states. (B and I) After one cycle at 0.1 C, 2.5 to 0.3 V, with the conventional 1 M LiTFSI:LiBETI electrolyte. (C and J) After 10 cycles at 0.1 C, 2.5 to 0.3 V, with the WIS electrolyte. (D to F and K to M) Higher-magnification SEM images of the electrodes in (A) to (C) and (H) to (J), respectively. EDS spectra collected on (**G**) $LiMn_2O_4$ electrodes and (**N**) LiV_3O_8 electrodes in pristine state after being cycled in the 1 M LiTFSI:LiBETI electrolyte and after being cycled in the WIS electrolyte.

and the dissolved Mn cations then redeposited onto the surface of the LiV_3O_8 anode. This dissolution observed in EDS analysis is also consistent with the surface morphological change observed in Fig. 3 (A to F), showing the severe dissolution of the $LiMn_2O_4$ particles when the cell is being cycled with the 1 M LiTFSI:LiBETI electrolyte. Similarly, in Fig. 3G, a V impurity peak is also observed in the EDS spectrum of the $LiMn_2O_4$ cathode from the cell with the 1 M LiTFSI:LiBETI electrolyte, indicating that LiV_3O_8 also dissolves when cycled in the conventional 1 M electrolyte due to the water-involved side reaction. In the same plots, with the WIS electrolyte, Mn Kα peak is not observed on the anode, and a much less intense V Kα peak is observed on the cathode. On the basis of these observations, it can be established that the WIS electrolyte also suppresses the active material dissolution and corrosion in the aqueous Li-ion battery. The reason for this effect should be rooted in the exhausted coordination power of water molecule when it is nominally a solute in the WIS electrolyte (*6*). Nevertheless, the dissolved vanadium cations may travel between cathode and anode as a "shuttling process," which could degrade coulombic efficiency in the WIS battery (*32*). Overall, the coulombic efficiency is at the ~97% level for the WIS electrolyte system, which is higher than the 1 M dilute electrolyte (~70 to 80%). The better electrochemical stability in the WIS system involves the expansion of water voltage window, thus suppressing the active material dissolution.

Operando x-ray imaging of $LiMn_2O_4$ in conventional and WIS aqueous electrolytes

Operando TXM observation of the aqueous Li-ion cells with different electrolytes—WIS versus conventional aqueous electrolytes—was applied to provide a more detailed comparison of their electrochemical stability. Because of the overlap between the $LiMn_2O_4$ cathode and the LiV_3O_8 anode and the relatively weak absorption of the LiV_3O_8 particles, the observation was carried out under an imaging condition where the imaging contrast for $LiMn_2O_4$ is enhanced by controlling the incident x-ray energy. The x-ray energy was selected to be slightly above the Mn K-edge (6.539 keV), where the absorption contrast between the $LiMn_2O_4$ particles and the background is the greatest because of the onset of the Mn element's characteristic K-edge absorption. This is exemplified by the comparison between the transmission x-ray images collected below and above the Mn K-edge shown in fig. S3. With both the 1 M (1.2 m) LiTFSI:LiBETI electrolyte and the WIS electrolyte, there is a major increase in the overall absorption from below to above the Mn K-edge. The particles with round shape resemble the spherical $LiMn_2O_4$ particles shown in the SEM images in fig. S2. The operando study focuses on analyzing the morphological evolution of these particles and the corresponding clusters.

The operando x-ray images were converted to the x-ray attenuation by taking the negative logarithm of the background-normalized images. To provide a better visualization of the operando x-ray imaging,

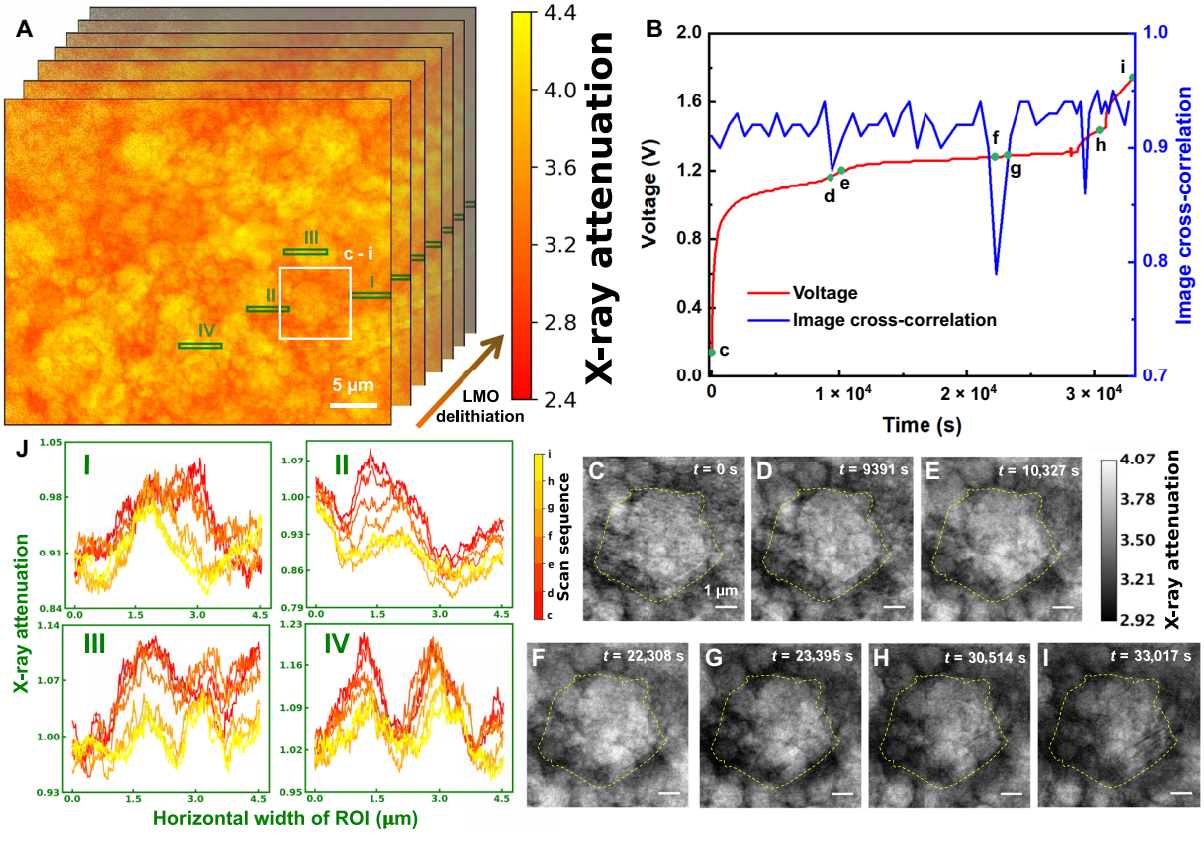

Fig. 4. Operando imaging of LiV_3O_8-$LiMn_2O_4$ cell with the 1 M LiTFSI:LiBETI conventional aqueous electrolyte. (**A**) Image stack of delithiation. (**B**) Voltage profile of the cell and the image cross-correlation calculated by *n* frame and *n* + 1 frame, with *n* being the index of any given frame. (**C** to **I**) The TXM operando images collected from the cell at different time points labeled in (B). The particle displayed in (C) to (I) is marked with a white square in (A). (**J**) Decrease in x-ray attenuation during charging as particle undergoes a dissolution process. The ROIs displayed in (I) to (IV) are marked with green rectangles in (A); the color scales correspond to specific cycling state, as marked by (c-i). Videos of the full series of operando images including the full frame and the individual particle can be found in the Supplementary Materials.

the images recorded during the experiment were processed into videos and correlated with the voltage profiles of the Li-ion batteries cycled in situ during the operando x-ray imaging experiments. The video for the 1 M LiTFSI:LiBETI electrolyte cell is shown in movie S1, and the one for the WIS electrolyte is shown in movie S2. The corresponding voltage profiles and several snapshots of the videos are also shown in Figs. 4 and 5 or in figs. S4 and S5.

As mentioned in the experimental section, the cells were cycled at a rate of 0.2 C, normalized to $LiMn_2O_4$ capacity. Assuming 100% utilization of the $LiMn_2O_4$ at this rate, theoretically, the full charge and discharge will take 10 hours. However, after the 1 M LiTFSI:LiBETI cell had been charged for more than 8 hours at 0.2 C, it was still far below the cutoff voltage of 2 V. Because of the limited beam time, the rate was then increased to 0.5 C at 7.9 hours and to 1.0 C at 8.7 hours consecutively to expedite the process, which still failed to enable the cell to reach 2 V within the experiment time allocated. This charging behavior is similar to the infinite charging observed in Fig. 2A. Note that the operando cell took remarkably longer time to traverse the 1.2- to 1.3-V range at 0.2 C, which was not a major issue for the coin cell with the 1 M LiTFSI:LiBETI electrolyte cycled at a rate of 0.1 C (Fig. 2A). This might be caused by the inherent instability of the 1 M LiTFSI:LiBETI electrolyte that generates variation from cell to cell.

On the other hand, the operando cell with the WIS electrolyte behaved consistently during the charge-discharge cycle, which resembles the profile in Fig. 2C in overall shape, despite the slightly lower capacity of 117 mAh g^{-1} delivered at 0.2 C. Overall, the performance of the operando cells used for in situ TXM is consistent with the ex situ results, in which the WIS electrolyte shows a much more efficient charging process and better recovery of the particle morphology.

A comparison of the two videos provides two overall observations: (i) The particles in the electrode in the 1 M LiTFSI:LiBETI electrolyte cell were repositioning during the cycling, whereas in the WIS electrolyte cell, the particles did not experience much movement; (ii) the particles in the WIS electrolyte cell shrank in size during the charge and recovered during the discharge reversibly, but in the 1 M LiTFSI:-LiBETI electrolyte cell, the size reduction of the particles during the charging was accompanied by substantial contrast loss. The critical voltage points, where different morphological changes occurred in the 1 M LiTFSI:LiBETI electrolyte cell, are shown in Fig. 4B, along with the corresponding snapshots in Fig. 4 (C to I). For the WIS electrolyte, in Fig. 5B, the voltage points were chosen at the boundaries between different voltage plateaus during the charge and discharge.

In the 1 M LiTFSI:LiBETI electrolyte cell, the first major collective particle motion happened between 1.16 and 1.20 V, as illustrated by the comparison between Fig. 4, D and E, while from the beginning of the cycle to 0.14 V in Fig. 4C to 1.16 V in Fig. 4D, there was no visible position change among the particles. This type of electrode particle motion is expected to lead to mechanical damage to the electrode and affect the active material utilization and cycle life. The

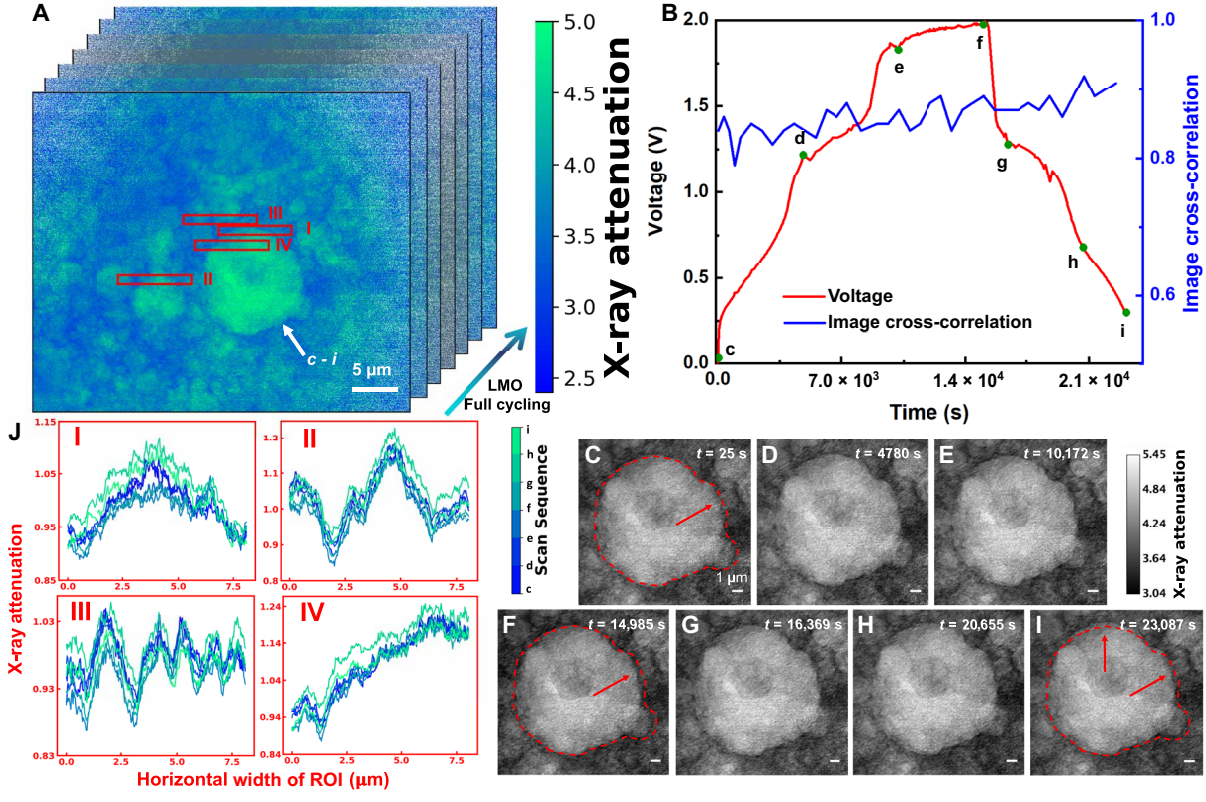

Fig. 5. Operando imaging of LiV_3O_8-$LiMn_2O_4$ cell with the WIS electrolyte. (**A**) Image stack of full cycling. (**B**) Voltage profile of the cell and the image correlation calculated by *n* frame and *n* + 1 frame, with *n* being the index of any given frame. (**C** to **I**) The TXM operando images collected from the cell at the different time points labeled in (B). The particle displayed in (C) to (I) is marked with a white arrow in (A). (**J**) Evolutions of x-ray attenuation during a full cycle as particle shrinks in charging and expands in discharging. The ROIs displayed in (I) to (IV) are marked with red rectangles in (A); the color scales correspond to specific cycling state, as marked by (c-i). Videos of the full series of operando images including the full frame and the individual particle can be found in the Supplementary Materials.

voltage of this major particle motion is also very close to the electrochemical window of water (~1.23 V). Although during the operando experiment no bubble formation was ever observed in the microscope, the particle motion observed here, which happened close to the voltage window of H_2O, might be related to water decomposition. The other major particle motion happened between 1.28 V in Fig. 4F and 1.29 V in Fig. 4G. Afterward, there was no major particle repositioning until the end of test at 1.74 V. The repositioning of the electrode particles in the 1 M LiTFSI:LiBETI electrolyte cell can be further quantified by the changes of image cross-correlation shown in Fig. 4B. Two relative low-image correlation points that resulted from particle reposition coincide with Fig. 4 (D to G).

Besides particle motion, the morphological change of individual particles can also be observed. From Fig. 4 (C to I), the zoom-in view of a particle, which is marked with a white square in Fig. 4A, experienced substantial volume shrinkage and contrast loss. This trend is also observed in different regions of interest (ROIs) marked with green rectangles in Fig. 4A. With the corresponding integrated x-ray attenuation in Fig. 4J, the x-ray attenuation was decreasing during the delithiation of the $LiMn_2O_4$ electrode. Although the volume shrinkage is generally expected for a $LiMn_2O_4$ particle during delithiation (*33*), the contrast loss is much more pronounced, presenting evidence of the onset of other processes, such as the $LiMn_2O_4$ dissolution, which is observed in the ex situ SEM images in Fig. 3. From Fig. 4 and movie S1, the contrast loss of the particle primarily happened after the voltage reaches 1.2 V, which is close to the electrochemical window of water. On the basis of this, it is inferred that $LiMn_2O_4$'s dissolution is the aftermath of water decomposition. This might be due to the consumption of OH^- by O_2 evolution on the cathode, which increases the concentration of H^+ locally and leads to the corrosion of $LiMn_2O_4$.

From the image correlation with the voltage profile in Fig. 5B, it is again demonstrated that the morphological change of the $LiMn_2O_4$ particles in the WIS electrolyte cell is much less significant compared to the 1 M LiTFSI:LiBETI electrolyte. No relative particle motion has been observed, and the particles' contrast in the x-ray images remained consistent during cycling. This is evidence that the WIS electrolyte is much more stable and does not interfere with the electrode's mechanical stability and the individual particles' electrochemical stability when working under adverse electrochemical bias. The only change observed in Fig. 5 is the particle size change with the voltage profile, which is relatively subtle but can still be analyzed through the particle labeled with a white arrow in Fig. 5A and zoom-in view in Fig. 5 (C to I). In Fig. 5 (C, F, and I), the red dashed lines (same size in three images) and arrows are labeled to highlight the particle size change; a subtle particle shrinkage in Fig. 5F can be observed, and this was recovered as seen in Fig. 5I. The shrinkage and recovery of particle size are also quantified for different ROIs marked with red rectangles in Fig. 5A; the changes of x-ray attenuation profile in each ROI are shown in Fig. 5J. The x-ray attenuation decreases during charging and then increases during discharging, corresponding to the reduction and expansion of particle size during cycling. The area of the particle in Fig. 5 was measured and plotted in fig. S6. The approximated area of the labeled particle is 101.6 μm^2 (100%) at the beginning of the test, consistently shrinks to 92.6 μm^2 (91.1%) at the end of the charge at 2 V due to delithiation, and finally recovers to 100.2 μm^2 (98.6%) at the end of discharge at 0.3 V due to lithiation. The size evolution here shows good reversibility of the cell with the WIS electrolyte. The volume deficit of this cycle is also consistent with the capacity loss of the discharge relative to the charge in Fig. 5B, which is probably associated with the irreversible capacity contributed by the anode SEI formation (*6*, *8*–*10*).

Chemical heterogeneity of electrodes in WIS system

Because of the 100 times larger viscosity of the WIS electrolyte than the 1 M (1.2 m) LiTFSI:LiBETI electrolyte shown in fig. S10, understanding the limitation of transport by mapping chemical heterogeneity is crucial. To visualize the chemical reactions at different states, XANES spectroscopic imaging was conducted on postcycled $LiMn_2O_4$ cathodes in the WIS system. A tomographic reconstruction of the focused ion beam (FIB)–milled $LiMn_2O_4$ is shown in Fig. 6A, where the orientations of the electrode surface and current collector are labeled; this allows us to better understand the origin of the chemical heterogeneity. Figure 6 (B to D) shows the mappings of chemical states, represented by the white line positions where x-ray absorption

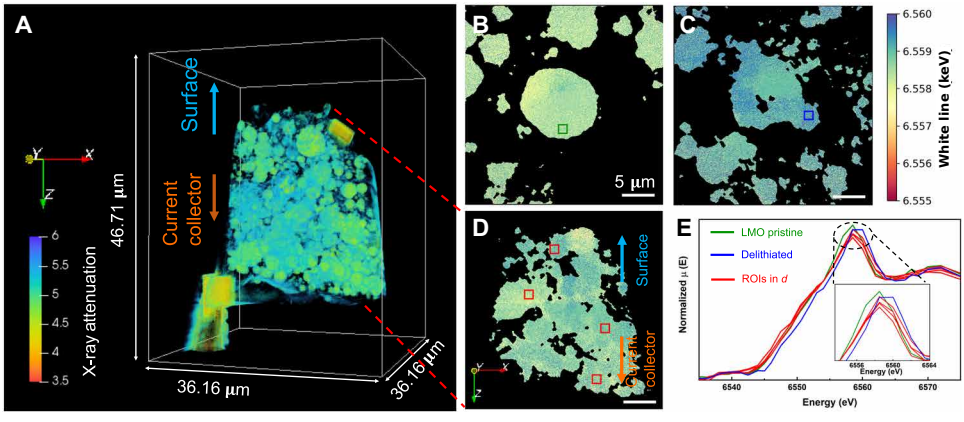

Fig. 6. 3D tomography and 2D XANES spectroscopic mapping of various states of $LiMn_2O_4$ electrodes in WIS system. (**A**) 3D nanotomographic reconstruction of a 20-μm electrode, fully charged (delithiated) at a rate of 0.5 C. (**B**) $LiMn_2O_4$ pristine state. (**C**) Ten-micrometer electrode, fully charged (delithiated) at a rate of 0.1 C, which delivered ~100% theoretical capacity. (**D**) Twenty-micrometer electrode, fully charged at a rate of 0.5 C, which delivered 85% theoretical capacity. Note that (D) is the projection of (A) at the *x*-*z* plane. (**E**) XANES spectra of selected regions (30 × 30 pixels) in (B) to (D); inset figure shows the spectra at the white line positions, which correspond to the oxidation state changes in the electrodes.

spectroscopy (XAS) has a maximum attenuation, of three different electrodes. Figure 6B is the pristine LiM_2O_4 electrode that represents the initial condition; Fig. 6C [10 μm; $LiMn_2O_4$ loading: 1.4 mg cm^{-2}] is the fully charged $LiMn_2O_4$ electrode cycled at a rate of 0.1 C, which delivered ~100% of $LiMn_2O_4$ (theoretical capacity representing a condition that has minimal kinetic effect). Figure 6D is the same sample as Fig. 6A but imaged via the 2D XANES mode. The sample shown in Fig. 6 (A and D) (20 μm; $LiMn_2O_4$ loading: 2.3 mg cm^{-2}) is a fully charged $LiMn_2O_4$ electrode, which reacted at a faster 0.5-C rate and with a thicker electrode in comparison to the sample shown in Fig. 6C (20 μm versus 10 μm); electrochemical testing (fig. S7) demonstrated that the $LiMn_2O_4$ electrode shown in Fig. 6D delivered ~85% capacity, despite the moderate cycling rate. During the charging/delithiation process, Mn of $LiMn_2O_4$ is being oxidized, and hence, the white line position shifts toward higher energy (*34*). Qualitatively, the chemical mapping of the 20-μm electrode in Fig. 6D shows more heterogeneous chemical states with less completed reaction than the fully delithiated case in Fig. 6C. This observation agrees with the electrochemical result. To understand the transport limitations, some ROIs at different positions along the thickness direction of the electrode are selected in Fig. 6D, and their XANES spectra are plotted in Fig. 6E. The spectra of selected ROIs in Fig. 6E (colored in red) do not show clear difference of chemical states from the surface of the electrode to the current collector. Although the $LiMn_2O_4$ electrode in Fig. 6D delivered ~85% capacity, the effect of chemical heterogeneity is still not significant likely because of the porous structure and the relative thin electrode. This suggests that to understand the limitation of the transport and kinetic effect, further investigations are required to be carried out with even thicker electrodes. The porosity may also be controlled via calendaring to investigate the effect of the porous structure on the kinetic limitations of the WIS electrolyte. In addition, a systematic investigation to understand the contribution of different thicknesses and cycling rates would be critical to reveal the potential kinetic limitation of the WIS system.

CONCLUSION

In summary, a cell chemistry based on LiV_3O_8 as the anode and $LiMn_2O_4$ as the cathode was demonstrated showing improved performance in the WIS electrolyte system relative to 1 M salt in an aqueous Li-ion battery. On the basis of the SEM study and the operando TXM study, the stabilization effect of the WIS electrolyte is a combination of suppressing the water decomposition and preventing active material dissolution, especially the $LiMn_2O_4$ cathode, during the charging process at relatively high voltages. Operando x-ray imaging quantifies the evolution of particle size via x-ray attenuation profiling on individual particles and of the particle motion via image cross-correlation of consecutive image frames.

These results indicate that there is significant mechanical damage toward the electrode's particle network during the charging process in the conventional dilute (1 M) concentration aqueous electrolyte at high voltages (>1.3 V). The mechanical damage of the electrode might be associated with the water decomposition process, which disrupts the electrode and causes the movement of the electrode particles. In comparison, the electrode cycled in the WIS electrolyte displays a stable electrode network, and the particle size change—shrinkage and expansion—was reversible during the charge and discharge. The chemical heterogeneity in a cycled electrode in the WIS electrolyte was revealed in the XANES spectroscopic imaging. The 2D XANES spectroscopic imaging visualizes the chemical heterogeneity on a partially delithiated electrode cycled in WIS. A more systematic investigation is required to fully understand and further mitigate the kinetic limits and transport phenomena of the WIS system. For example, even thicker and denser electrodes shall be considered to study the transportation limits. In addition, single crystal particles can be studied to address more fundamental reaction mechanisms in battery reaction for the WIS system (*35*, *36*). Addressing the transport limitations of the WIS electrolyte and enhancing the kinetics of the charge-carrying ions in the WIS electrolyte without compromising its superior stability will likely have a great impact in the aqueous battery field and potentially the broader field of energy storage and conversion systems.

MATERIALS AND METHODS

Electrode preparation, half-cell performance test, and characterization

LiV_3O_8 was synthesized with a sol-gel method as previously reported (*28*). $LiMn_2O_4$ powder and H_2O [high performance liquid chromatography (HPLC) grade] were both obtained from Sigma-Aldrich. LiTFSI and LiBETI were purchased from Tokyo Chemical Industry. XRD of LiV_3O_8 and $LiMn_2O_4$ was conducted using a Rigaku SmartLab x-ray diffractometer using copper K-α radiation. SEM imaging of the raw $LiMn_2O_4$ and LiV_3O_8 powders was done using a JEOL 7600 SEM.

Aprotic electrolyte used in this study was 1 M (mol L^{-1}) $LiPF_6$ in ethylene carbonate (EC):dimethyl carbonate (DMC) = 1:1 (v/v) obtained from MTI Corporation. Aqueous electrolyte with 1 M lithium composite salt was prepared using a mixture of LiTFSI and LiBETI in water with 1.2 m (mol kg^{-1}). The WIS electrolyte was prepared by dissolving LiTFSI and LiBETI in water with 27.8 m, with a molar ratio of LiTFSI:LiBETI = 7:3 (*9*). The viscosity of two electrolytes was acquired as a function of shear rate (10 to 500 s^{-1}) in a logarithmically flow sweep mode by using a TA Discovery HR-3 rheometer.

To conduct the half-cell performance test of the raw materials' electrochemical property and of the behavior of the LiV_3O_8-$LiMn_2O_4$ couple in different aqueous electrolytes, electrodes were prepared with a conventional tape-casting method. The active material powders were vortex mixed in a planetary mixer with carbon black (Super C65) and binder (polyvinylidene difluoride, Alfa Aesar) in 1-methyl-2-pyrrolidone (NMP) to form the electrode slurries. The composition of the slurries was active material:Super C65:polyvinylidene difluoride in a ratio of 85:10:5 by weight. The slurry was casted onto thin metal foils with a doctor blade. The current collector for $LiMn_2O_4$ was titanium (Sigma-Aldrich), and the one for LiV_3O_8 was aluminum (MTI). To test the half-cell performance of the $LiMn_2O_4$ and LiV_3O_8 electrodes, 2032 coin cells were assembled with $LiMn_2O_4$ or LiV_3O_8 as the cathode and lithium metal as the anode. The electrolyte for the baseline half-cell test was 1 M $LiPF_6$ in EC:DMC = 1:1 (v/v). For full-cell test with the aqueous electrolytes, $LiMn_2O_4$ was directly paired with LiV_3O_8 in the 2032 type coin cells. The capacity ratio of $LiMn_2O_4$:LiV_3O_8 was ~0.8 to 0.9 in the full cell. Because the capacity was always cathode limited, the capacity of the cell was normalized to the weight of the $LiMn_2O_4$ for an easier comparison between different tests. The performance was tested in different electrolytes: the conventional 1 M (1.2 m) LiTFSI:LiBETI electrolyte and the WIS electrolyte. The separator used in the coin cell tests was Celgard 2325.

Charge and discharge tests were done using an Arbin BT2000 battery tester. Cycling rates for the half-cell tests were 0.1, 1, 2, and 5 C, with voltage ranges of 1.6 to 4.0 V for LiV_3O_8 and 3.5 to 4.5 V for $LiMn_2O_4$. Cycling rates for the LiV_3O_8-$LiMn_2O_4$ full test were 0.1 and 1 C, and the voltage range was 0.3 to 2.5 V or 0.3 to 2.0 V. Postcycling SEM and EDS were done on the electrodes with JEOL 7600 SEM at a bias of 15 keV.

Synchrotron operando nanoimaging of $LiMn_2O_4$ morphological evolution in aqueous electrolytes

The synchrotron operando TXM study was conducted at the Full-Field X-ray Imaging Beamline (*37*) (FXI, 18-ID) of National Synchrotron Light Source II (NSLS-II) at the Brookhaven National Laboratory. The TXM at FXI Beamline provided a field of view of 41.6 μm × 35.1 μm ($h \times v$) with a pixel size of 32.5 nm during operando measurement in this study; the optical resolution of the microscope is ~30 nm under binning 1 condition, which was critical to resolve the fine features in the studied systems. A schematic and a photo showing the layout of the experimental setup experiment are shown in Fig. 1. The operando coin cells (2032 type) had a circular opening of 2 mm diameter in the center to allow the x-ray transmission. Both 1 M (1.2 m) LiTFSI:LiBETI and WIS electrolytes were studied by operando TXM imaging. During the operando TXM study, the LiV_3O_8-$LiMn_2O_4$ coin cells were charged and discharged for one cycle between 2.0 and 0.3 V, controlled by a Bio-Logic VMP3 potentiostat. For the WIS electrolyte cell, the rate was 0.2 C, normalized by the capacity of the $LiMn_2O_4$ theoretical capacity value, 140 mAh g^{-1} (*38*). For the 1 M electrolyte cell, the rate was 0.2 C from the beginning to 7.9 hours, 0.5 C from 7.9 to 8.7 hours, and 1 C until the end of the test. The rate change was performed to accommodate the beamtime time limitations but not to affect the observations presented in this study. The operando TXM images were collected at x-ray energies just above the Mn K-edge (6.539 keV) to maximize the contrast for $LiMn_2O_4$ cathode materials. The cells were also examined below and above the Mn and V edges to ensure that the particles studied during the operando studies were $LiMn_2O_4$ particles. The interval between each image collection was 10 min, with an exposure time of 1.5 to 2 s, to ensure that the beam intensity is consistent across experiments.

Operando imaging series were first aligned by freeware ImageJ (Fiji) (*39*) with StackReg plugin (*40*) to ensure that only the relative particle motion was analyzed. Then, the images were converted to the x-ray attenuation by calculating the negative natural logarithm of every pixel. Each frame was then normalized by the total attenuation of a given frame to normalize the beam intensity fluctuation that could not be accounted for in the flat-field correction. To quantify the evolution of particle morphology, several ROIs were selected; the x-ray attenuation profiles were plotted as a function of time, which also corresponded to electrochemical cycles, along the horizontal direction, with a 30-pixel width along the vertical direction. The image cross-correlation coefficient was calculated between n and $n + 1$ frame of the operando imaging series in freeware ImageJ (Fiji) (*39*) with a package, Image CorrelationJ (*41*); n represented the index of any given frame.

Synchrotron spectroscopic imaging to study kinetic effects in the WIS electrolyte

2D XANES spectroscopic imaging of postcycled $LiMn_2O_4$ electrodes with the WIS electrolyte was also conducted at the FXI beamline of NSLS-II to study the evolution of chemical states. A series of 2D XANES images was collected at each electrode for fully lithiated and delithiated states. Each set of 2D XANES images was obtained by scanning the Mn K-edge from 6.457 to 6.820 keV. The cells were prepared to study in the fully charged state (2.0 V) and in the fully discharged state after one full cycle (open circuit voltage to 2.0 V for charging and discharged to 0.3 V); all cells were cycled under 0.1- and 0.5-C rates, normalized to the capacity of $LiMn_2O_4$. The postcycled XANES samples were collected by disassembling coin cells and sealed in Kapton films after drying under vacuum for 24 hours before the experiments at FXI beamline. FIB-SEM lift-out was conducted, following the procedure developed previously (*42*), to prepare one $LiMn_2O_4$ electrode (20 μm, 0.5 C) to differentiate the chemical states between the surface and interior of the electrode. The conditions of the FIB-SEM lift-out procedure and the schematic experimental setup of ex situ measurements (fig. S9) can be found in the Supplementary Materials. All the XANES data were first processed using PyXAS, an in-house Python package with graphic user interface developed at FXI beamline of NSLS-II by M.G., to align the XANES image stacks and generate mask to filter nonactive components in the images. The chemical states of each pixel were then determined by identifying the white line energy positions from the spectroscopic images, which corresponds to the energies with maximum x-ray attenuation. The standard spectra, including pristine $LiMn_2O_4$ and fully discharged (delithiated) $LiMn_2O_4$, were also measured on TXM at 18-ID, NSLS-II, with the same conditions as 2D XANES images. The reference materials after lithiation/delithiation were prepared through the battery reaction with conventional organic electrolyte (1 M $LiPF_6$ in EC:DMC = 1:1) in coin cell; the reaction products were previously reported (*28*, *30*).

SUPPLEMENTARY MATERIALS

Supplementary material for this article is available at http://advances.sciencemag.org/cgi/content/full/6/10/eaay7129/DC1

The conditions of FIB-SEM lift-out procedure

Fig. S1. Characterizations of LiV_3O_8 powder and LiV_3O_8 half-cell.

Fig. S2. Characterizations of $LiMn_2O_4$ powder and $LiMn_2O_4$ half-cell.

Fig. S3. TXM images of $LiMn_2O_4$-LiV_3O_8 cell with the 1 M LiTFSI:LiBETI and WIS electrolyte collected above and below Mn K-edge.

Fig. S4. Voltage profile versus TXM images of the operando LiV_3O_8-$LiMn_2O_4$ cell with the 1 M LiTFSI:LiBETI electrolyte.

Fig. S5. Voltage profile versus TXM images of the operando LiV_3O_8-$LiMn_2O_4$ cell with the WIS electrolyte.

Fig. S6. Measured area change of the tagged particle with the operando cell's depth of discharge in Fig. 5.

Fig. S7. The electrochemical profiles of two cells which $LiMn_2O_4$ electrodes were XANES imaged in Fig. 6.

Fig. S8. The high-resolution SEM images corresponding to Fig. 3 (B and E).

Fig. S9. The experimental setup for tomography and 2D XANES imaging.

Fig. S10. The viscosity as a function of shear rate for the WIS electrolyte and the 1 M LiTFSI:LiBETI electrolyte.

Fig. S11. Graphical abstract.

Movie S1. Video of the full frame of 1 M aqueous electrolyte cell—Full field of view.

Movie S2. Video of the full frame of 1 M aqueous electrolyte cell—Individual particle.

Movie S3. Video of the full frame of the WIS electrolyte cell—Full field of view.

Movie S4. Video of the full frame of the WIS electrolyte cell—Individual particle.

Movie S5. Nanotomography of 20-μm-thick $LiMn_2O_4$ electrode cycled in the WIS electrolyte.

REFERENCES AND NOTES

1. W. Li, J. R. Dahn, D. S. Wainwright, Rechargeable lithium batteries with aqueous-electrolytes. *Science* **264**, 1115–1118 (1994).
2. H. Kim, J. Hong, K.-Y. Park, S.-W. Kim, K. Kang, Aqueous rechargeable Li and Na Ion Batteries. *Chem. Rev.* **114**, 11788–11827 (2014).
3. J.-Y. Luo, Y.-Y. Xia, Aqueous lithium-ion battery $LiTi_2(PO_4)_3$/$LiMn_2O_4$ with high power and energy densities as well as superior cycling stability. *Adv. Funct. Mater.* **17**, 3877–3884 (2007).

4. J.-Y. Luo, W.-J. Cui, P. He, Y.-Y. Xia, Raising the cycling stability of aqueous lithium-ion batteries by eliminating oxygen in the electrolyte. *Nat. Chem.* **2**, 760–765 (2010).
5. W. Wu, S. Shanbhag, A. Wise, J. Chang, A. Rutt, J. F. Whitacre, High performance TiP_2O_7 based intercalation negative electrode for aqueous lithium-ion batteries via a facile synthetic route. *J. Electrochem. Soc.* **162**, A1921–A1926 (2015).
6. L. M. Suo, O. Borodin, T. Gao, M. Olguin, J. Ho, X. L. Fan, C. Luo, C. S. Wang, K. Xu, "Water-in-salt" electrolyte enables high-voltage aqueous lithium-ion chemistries. *Science* **350**, 938–943 (2015).
7. L. Suo, F. Han, X. Fan, H. Liu, K. Xu, C. Wang, "Water-in-salt" electrolytes enable green and safe Li-ion batteries for large scale electric energy storage applications. *J. Mater. Chem. A* **4**, 6639–6644 (2016).
8. L. M. Suo, O. Borodin, W. Sun, X. L. Fan, C. Y. Yang, F. Wang, T. Gao, Z. H. Ma, M. Schroeder, A. von Cresce, S. M. Russell, M. Armand, A. Angell, K. Xu, C. S. Wang, Advanced high-voltage aqueous lithium-ion battery enabled by "water-in-bisalt" electrolyte. *Angew. Chem. Int. Ed. Engl.* **55**, 7136–7141 (2016).
9. Y. Yamada, K. Usui, K. Sodeyama, S. Ko, Y. Tateyama, A. Yamada, Hydrate-melt electrolytes for high-energy-density aqueous batteries. *Nat. Energy* **1**, 16129 (2016).
10. W. Sun, L. M. Suo, F. Wang, N. Eidson, C. Y. Yang, F. D. Han, Z. H. Ma, T. Gao, M. Zhu, C. S. Wang, "Water-in-salt" electrolyte enabled $LiMn_2O_4/TiS_2$ lithium-ion batteries. *Electrochem. Commun.* **82**, 71–74 (2017).
11. C. Yang, J. Chen, T. Qing, X. Fan, W. Sun, A. von Cresce, M. S. Ding, O. Borodin, J. Vatamanu, M. A. Schroeder, N. Eidson, C. Wang, K. Xu, 4.0 V aqueous Li-Ion batteries. *Joule* **1**, 122–132 (2017).
12. M. R. Lukatskaya, J. I. Feldblyum, D. G. Mackanic, F. Lissel, D. L. Michels, Y. Cui, Z. A. Bao, Concentrated mixed cation acetate "water-in-salt" solutions as green and low-cost high voltage electrolytes for aqueous batteries. *Energ. Environ. Sci.* **11**, 2876–2883 (2018).
13. Q. Dong, X. Yao, Y. Zhao, M. Qi, X. Zhang, H. Sun, Y. He, D. Wang, Cathodically stable Li-O_2 battery operations using water-in-salt electrolyte. *Chem* **4**, 1345–1358 (2018).
14. J. Han, H. Zhang, A. Varzi, S. Passerini, Fluorine-free water-in-salt electrolyte for green and low-cost aqueous sodium-ion batteries. *ChemSusChem* **11**, 3704–3707 (2018).
15. D. P. Leonard, Z. X. Wei, G. Chen, F. Du, X. L. Ji, Water-in-salt electrolyte for potassium-ion batteries. *ACS Energy Lett.* **3**, 373–374 (2018).
16. X. Wu, Y. Xu, C. Zhang, D. P. Leonard, A. Markir, J. Lu, X. Ji, Reverse dual-ion battery via a ZnCl2 water-in-salt electrolyte. *J. Am. Chem. Soc.* **141**, 6338–6344 (2019).
17. Z. Tian, W. Deng, X. Wang, C. Liu, C. Li, J. Chen, M. Xue, R. Li, F. Pan, Superconcentrated aqueous electrolyte to enhance energy density for advanced supercapacitors. *Funct. Mater. Lett.* **10**, 1750081 (2017).
18. X. Liu, D. Vonk, H. Jiang, K. Kisslinger, X. Tong, M. Ge, E. Nazaretski, B. Ravel, K. Foster, S. Petrash, Y.-c. K. Chen-Wiegart, Environmentally friendly Zr-based conversion nanocoatings for corrosion inhibition of metal surfaces evaluated by multimodal x-ray analysis. *ACS Appl. Nano Mater.* **2**, 1920–1929 (2019).
19. J. Nelson, S. Misra, Y. Yang, A. Jackson, Y. J. Liu, H. Wang, H. Dai, J. C. Andrews, Y. Cui, M. F. Toney, In operando x-ray diffraction and transmission x-ray microscopy of lithium sulfur batteries. *J. Am. Chem. Soc.* **134**, 6337–6343 (2012).
20. S. Müller, P. Pietsch, B.-E. Brandt, P. Baade, V. De Andrade, F. De Carlo, V. Wood, Quantification and modeling of mechanical degradation in lithium-ion batteries based on nanoscale imaging. *Nat. Commun.* **9**, 2340 (2018).
21. J. Wang, Y.-c. K. Chen-Wiegart, J. Wang, In situ chemical mapping of a lithium-ion battery using full-field hard x-ray spectroscopic imaging. *Chem. Commun.* **49**, 6480–6482 (2013).
22. J. Wang, Y.-c. K. Chen-Wiegart, J. Wang, In operando tracking phase transformation evolution of lithium iron phosphate with hard x-ray microscopy. *Nat. Commun.* **5**, 4570 (2014).
23. L. Li, Y.-c. K. Chen-Wiegart, J. Wang, P. Gao, Q. Ding, Y.-S. Yu, F. Wang, J. Cabana, J. Wang, S. Jin, Visualization of electrochemically driven solid-state phase transformations using operando hard x-ray spectro-imaging. *Nat. Commun.* **6**, 6883 (2015).
24. J. Wang, Y.-c. K. Chen-Wiegart, C. Eng, Q. Shen, J. Wang, Visualization of anisotropic-isotropic phase transformation dynamics in battery electrode particles. *Nat. Commun.* **7**, 12372 (2016).
25. C. Zhao, T. Wada, V. De Andrade, D. Gürsoy, H. Kato, Y.-c. K. Chen-Wiegart, Imaging of 3D morphological evolution of nanoporous silicon anode in lithium ion battery by x-ray nano-tomography. *Nano Energy* **52**, 381–390 (2018).
26. Y. Xu, E. Hu, K. Zhan, X. Wang, V. Borzenets, Z. Sun, P. Pianetta, X. Yu, Y. Liu, X.-Q. Yang, H. Li, In situ visualization of state-of-charge heterogeneity within a $LiCoO_2$ particle that evolves upon cycling at different rates. *ACS Energy Lett.* **2**, 1240–1245 (2017).
27. D. A. Shapiro, Y.-S. Yu, T. Tyliszczak, J. Cabana, R. Celestre, W. Chao, K. Kaznatcheev, A. L. D. Kilcoyne, F. Maia, S. Marchesini, Y. S. Meng, T. Warwick, L. L. Yang, H. A. Padmore, Chemical composition mapping with nanometre resolution by soft x-ray microscopy. *Nat. Photonics* **8**, 765–769 (2014).
28. Q. Zhang, A. B. Brady, C. J. Pelliccione, D. C. Bock, A. M. Bruck, J. Li, V. Sarbada, R. Hull, E. A. Stach, K. J. Takeuchi, E. S. Takeuchi, P. Liu, A. C. Marschilok, Investigation of structural evolution of $Li_{1.1}V_3O_8$ by in situ x-ray diffraction and density functional theory calculations. *Chem. Mater.* **29**, 2364–2373 (2017).
29. Q. Zhang, A. M. Bruck, D. C. Bock, J. Li, E. A. Stach, E. S. Takeuchi, K. J. Takeuchi, A. C. Marschilok, Energy dispersive x-ray diffraction (EDXRD) of $Li_{1.1}V_3O_8$ electrochemical cell. *MRS Adv.* **2**, 401–406 (2017).
30. T. Ohzuku, M. Kitagawa, T. Hirai, Electrochemistry of manganese-dioxide in lithium nonaqueous cell: III. X-ray diffractional study on the reduction of spinel-related manganese-dioxide. *J. Electrochem. Soc.* **137**, 769–775 (1990).
31. S. J. B. Reed, N. G. Ware, Escape peaks and internal fluorescence in x-ray spectra recorded with lithium drifted silicon detectors. *J. Phys. E* **5**, 582 (1972).
32. C. Ding, H. Zhang, X. Li, T. Liu, F. Xing, Vanadium flow battery for energy storage: Prospects and challenges. *J. Phys. Chem. Lett.* **4**, 1281–1294 (2013).
33. K. Kanamura, H. Naito, T. Yao, Z.-i. Takehara, Structural change of the $LiMn_2O_4$ spinel structure induced by extraction of lithium. *J. Mater. Chem.* **6**, 33–36 (1996).
34. T. Okumura, Y. Yamaguchi, M. Shikano, H. Kobayashi, Further findings of x-ray absorption near-edge structure in lithium manganese spinel oxide using first-principles calculations. *J. Mater. Chem. A* **2**, 8017–8025 (2014).
35. Y.-S. Yu, C. Kim, Y. J. Liu, A. van der Ven, Y. S. Meng, R. Kostecki, J. Cabana, Nonequilibrium pathways during electrochemical phase transformations in single crystals revealed by dynamic chemical imaging at nanoscale resolution. *Adv. Energy Mater.* **5**, 1402040 (2015).
36. L. Hong, L. S. Li, Y.-K. Chen-Wiegart, J. Wang, K. Xiang, L. Gan, W. Li, F. Meng, F. Wang, J. Wang, Y.-M. Chiang, S. Jin, M. Tang, Two-dimensional lithium diffusion behavior and probable hybrid phase transformation kinetics in olivine lithium iron phosphate. *Nat. Commun.* **8**, 1194 (2017).
37. M. Ge, D. S. Coburn, E. Nazaretski, W. Xu, K. Gofron, H. Xu, Z. Yin, W.-K. Lee, One-minute nano-tomography using hard x-ray full-field transmission microscope. *Appl. Phys. Lett.* **113**, 083109 (2018).
38. H. Xia, Z. Luo, J. Xie, Nanostructured $LiMn_2O_4$ and their composites as high-performance cathodes for lithium-ion batteries. *Prog. Nat. Sci.* **22**, 572–584 (2012).
39. J. Schindelin, I. Arganda-Carreras, E. Frise, V. Kaynig, M. Longair, T. Pietzsch, S. Preibisch, C. Rueden, S. Saalfeld, B. Schmid, J.-Y. Tinevez, D. J. White, V. Hartenstein, K. Eliceiri, P. Tomancak, A. Cardona, Fiji: An open-source platform for biological-image analysis. *Nat. Methods* **9**, 676–682 (2012).
40. P. Thévenaz, U. E. Ruttimann, M. Unser, A pyramid approach to subpixel registration based on intensity. *IEEE Trans. Image Process.* **7**, 27–41 (1998).
41. G. Chinga, K. Syverud, Quantification of paper mass distributions within local picking areas. *Nord. Pulp Paper Res. J.* **22**, 441–446 (2007).
42. Y.-c. K. Chen-Wiegart, F. E. Camino, J. Wang, Sample preparation of energy materials for x-ray nanotomography with micromanipulation. *ChemPhysChem* **15**, 1587–1591 (2014).

Acknowledgments: We thank the Department of Materials Science and Chemical Engineering, the College of Engineering and Applied Sciences, and the Stony Brook University for the support. We thank the Chen-Wiegart group members—X. Liu, L. Zou, A. Ronne, and Q. Meng—for the support on sample preparation, data collection, and preliminary analysis during the FXI beamtime. We thank D. Bock for performing XRD characterization of the raw electrode materials. We thank the CFN staff, F. Camino and G. Wright, for the access and training on FIB-SEM and SEM/EDS, as well as D. Nykypanchuk for the access and training on rheological testing. **Funding:** This work was supported as part of the Center for Mesoscale Transport Properties (m2M/t), an Energy Frontier Research Center funded by the U.S. Department of Energy, Office of Science, Basic Energy Sciences, under award no. DE-SC0012673. This research used resources and FXI beamline (18-ID) of NSLS-II, a U.S. Department of Energy (DOE) Office of Science User Facility operated for the DOE Office of Science by Brookhaven National Laboratory under contract no. DE-SC0012704. This research used resources of the Center for Functional Nanomaterials (CFN), which is a U.S. DOE Office of Science Facility, at Brookhaven National Laboratory under contract no. DE-SC0012704. A.H.M. acknowledges the Graduate Assistance in Areas of National Need Fellowship (GAANN). E.S.T. acknowledges the support of William and Jane Knapp for the Knapp Chair in Energy and the Environment. **Author contributions:** K.S. and Y.-c.K.C.-W. developed the research concept with inputs from E.S.T. and A.C.M. C.-H.L., K.S., M.G., and Y.-c.K.C.-W. designed the synchrotron imaging experiments. C.-H.L. and K.S. prepared the WIS electrolyte and casting $LiMn_2O_4$ electrodes, assembled the electrochemical cells, and performed the cycling tests. K.S. performed the electrode analyses by SEM and EDS. L.M.H., A.H.M., and M.N.V. synthesized LiV_3O_8 powders and casted LiV_3O_8 electrodes under the supervision of K.J.T., E.S.T., and A.C.M. C.Z. conducted the FIB lift-out sample preparation for the kinetic

study. C.-H.L. conducted the rheological measurements on the electrolytes. C.-H.L., K.S., C.Z., and Y.-c.K.C.-W. conducted the synchrotron imaging experiments with the FXI beamline staff support by M.G., X.X., and W.-K.L. C.-H.L. and K.S. performed the imaging data analysis under the guidance of Y.-c.K.C.-W., M.G., and W.-K.L. C.-H.L. and K.S. wrote the manuscript under the supervision of Y.-c.K.C.-W., with inputs from all coauthors. **Competing interests:** The authors declare that they have no competing interests. **Data and materials availability:** All data needed to evaluate the conclusions in the paper are present in the paper and/or the Supplementary Materials. Additional data related to this paper may be requested from the authors.

Submitted 17 July 2019
Accepted 6 December 2019
Published 6 March 2020
10.1126/sciadv.aay7129

Citation: C.-H. Lin, K. Sun, M. Ge, L. M. Housel, A. H. McCarthy, M. N. Vila, C. Zhao, X. Xiao, W.-K. Lee, K. J. Takeuchi, E. S. Takeuchi, A. C. Marschilok, Y.-c. K. Chen-Wiegart, Systems-level investigation of aqueous batteries for understanding the benefit of water-in-salt electrolyte by synchrotron nanoimaging. *Sci. Adv.* **6**, eaay7129 (2020).

Science Advances

Systems-level investigation of aqueous batteries for understanding the benefit of water-in-salt electrolyte by synchrotron nanoimaging

Cheng-Hung Lin, Ke Sun, Mingyuan Ge, Lisa M. Housel, Alison H. McCarthy, Mallory N. Vila, Chonghang Zhao, Xianghui Xiao, Wah-Keat Lee, Kenneth J. Takeuchi, Esther S. Takeuchi, Amy C. Marschilok and Yu-chen Karen Chen-Wiegart

Sci Adv **6** (10), eaay7129.
DOI: 10.1126/sciadv.aay7129